

Inertia Induces Strong Orientation Fluctuations of Nonspherical Atmospheric Particles

T. Bhowmick^{1,2,*} J. Seesing^{1,*} K. Gustavsson^{3,*} J. Guettler¹ Y. Wang¹ A. Pumir^{4,1}
B. Mehlig³ and G. Bagheri^{1,†}

¹Max Planck Institute for Dynamics and Self-Organization, Göttingen, D-37077 Germany

²Institute for the Dynamics of Complex Systems, University of Göttingen,
Friedrich-Hund-Platz 1, Göttingen, D-37077 Germany

³Department of Physics, Gothenburg University, Gothenburg, SE-40530 Sweden

⁴Laboratoire de Physique, ENS de Lyon, Université de Lyon 1 and CNRS, Lyon, F-69007 France

 (Received 8 June 2023; revised 28 September 2023; accepted 22 November 2023; published 19 January 2024)

The orientation of nonspherical particles in the atmosphere, such as volcanic ash and ice crystals, influences their residence times and the radiative properties of the atmosphere. Here, we demonstrate experimentally that the orientation of heavy submillimeter spheroids settling in still air exhibits decaying oscillations, whereas it relaxes monotonically in liquids. Theoretical analysis shows that these oscillations are due to particle inertia, caused by the large particle-fluid mass-density ratio. This effect must be accounted for to model solid particles in the atmosphere.

DOI: [10.1103/PhysRevLett.132.034101](https://doi.org/10.1103/PhysRevLett.132.034101)

Introduction.—The transport, dispersion, and settling of volcanic ash [1,2], microplastic particles [3,4], and ice crystals in cold atmospheric clouds [5–8] have significant environmental impact. These nonspherical particles are subject to gravity, as well as viscous and inertial hydrodynamic forces and torques. An essential parameter characterizing the latter is the particle Reynolds number, defined by $Re_p = av_g/\nu$, where a is the linear size of the particle, v_g is its settling speed, and ν is the kinematic viscosity of air. In general, the transport of nonspherical particles depends strongly on their angular dynamics [9–11], which directly affects the settling speed [1,6,12,13]. This, in turn, determines its residence times and dispersion ranges in the atmosphere. The settling speed influences, for instance, how far microplastic, dust, and volcanic ash can be transported away from a source or how much time an ice crystal spends in a cloud [1–3,14]. In addition, the angular dynamics determines the volume swept out. Together with the settling speed, this volume is a key parameter determining particle-particle collision rates [15], e.g., relevant for the formation of aggregates of ice particles in clouds [16–19] or volcanic ash [2]. The particle orientation also has a direct impact on the absorption and scattering of radiation by the atmosphere, which affects the albedo of atmospheric clouds [20–22], an effect still not understood quantitatively, despite its importance [23–27].

Many studies investigated the drag and stable orientation of nonspherical particles settling in viscous liquids at rest [13,28–32], where the ratio $\mathcal{R} = \rho_p/\rho_f$ between the particle-mass density ρ_p and the fluid-mass density ρ_f is close to unity with $\mathcal{R} > 1$ (so the particle settles). In that case, when $Re_p \sim 10$, particle orientation aligns rapidly and monotonically, with its broad side down [11,33]. The angular dynamics becomes unsteady at larger Re_p . Settling particles in liquids, for example, exhibit a rich variety of motion patterns at $Re_p \sim 100$ [34]. In air with $\mathcal{R} \sim 1000$, the angular dynamics of thin settling disks exhibits bistability [35] at $Re_p \sim 50$. One expects that particle inertia plays an important role in explaining this qualitative difference, since \mathcal{R} is very large.

We remark that at much higher Re_p , the angular dynamics of nonspherical particles settling in still air becomes unstable [1]. Vortex shedding causes the characteristic fluttering first considered by Maxwell, see Ref. [36] and references cited there.

In turbulence, where fluid-velocity gradients give rise to additional torques, most experiments concern particles with $\mathcal{R} \approx 1$ [12,13,31,37–40]. Only a few experiments with turbulent fiber suspensions were carried out in air [41–43]. For the tumbling of heavy fibers in turbulence, particle inertia plays a role [39,44], but its effect remains to be quantified.

Experimentally, it remains a challenge to study the inertial angular dynamics of particles that settle very rapidly. One needs precise particle tracking over long periods of time, high-magnification imaging, a particle-release mechanism that does not set the fluid in motion, and the container must be large enough to avoid spurious interaction with the wall [30]. We developed a new

Published by the American Physical Society under the terms of the [Creative Commons Attribution 4.0 International license](https://creativecommons.org/licenses/by/4.0/). Further distribution of this work must maintain attribution to the author(s) and the published article's title, journal citation, and DOI. Open access publication funded by the Max Planck Society.

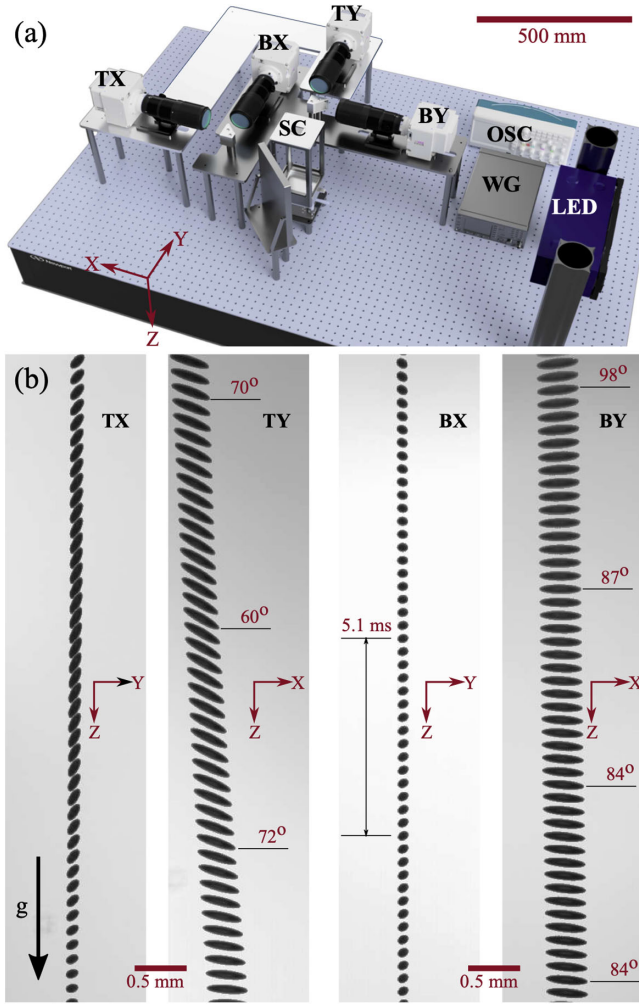


FIG. 1. Experimental setup. (a) Optical table with top cameras (TX and TY) and bottom cameras (BX and BY) named after the shown coordinate system (Z is the direction of gravity g), the settling chamber (SC), the synchronized pulsed LED unit, controlled with a waveform generator (WG), and the oscilloscope (OSC). (b) Snapshots of a settling prolate spheroid recorded at 2932 frames/s. The tilt angle—the angle between the particle symmetry axis and gravity—is shown in 5.1 ms intervals in units of degrees. See the Supplemental Material [45] for details.

experimental apparatus that overcomes these challenges [Fig. 1(a)]. Here we report on the first measurements, showing that the particle orientation exhibits characteristic oscillations with timescales comparable to those of atmospheric turbulence. The particles—with Re_p between 2 and 35—do eventually align so that they settle with their broad side down. We explain that the oscillations are induced by particle inertia, an effect that can significantly enhance the extent to which turbulence randomizes particle orientation.

Experiments.—The setup consists of an air-filled settling chamber with a novel particle injector and two high-speed camera pairs (TX, TY) and (BX, BY), synchronized with a high-intensity pulsed light-emitting diode (LED)

TABLE I. Size groups of particles studied. Parameters: aspect ratio $\lambda = a_{\parallel}/a_{\perp}$ ($2a_{\parallel}$ is the particle length along its symmetry axis, and $2a_{\perp}$ is its diameter); volume V_p ; Reynolds number Re_p (using $a = \max\{a_{\parallel}, a_{\perp}\}$ and the observed settling speed); Stokes time $\tau_p = (2\rho_p/9\rho_f)a_{\perp}a_{\parallel}/\nu$, where ρ_p and ρ_f are the mass densities of the particle and the fluid, and $\nu = 1.5 \times 10^{-5} \text{ m}^2/\text{s}$ is the kinematic viscosity of air.

| Group | λ | $2a_{\parallel}$ (μm) | $2a_{\perp}$ (μm) | V_p (mm^3) | Re_p | τ_p (ms) |
|-------|-----------|------------------------------------|--------------------------------|-------------------------|--------|---------------|
| I | 0.20 | 47.9 | 239.4 | 1.44×10^{-3} | 2.8 | 42.0 |
| I | 0.50 | 88.2 | 176.4 | 1.44×10^{-3} | 2.5 | 57.0 |
| I | 0.80 | 120.6 | 150.8 | 1.44×10^{-3} | 2.4 | 66.7 |
| I | 1.00 | 140.0 | 140.0 | 1.44×10^{-3} | 2.2 | 71.8 |
| I | 1.25 | 162.0 | 130.0 | 1.44×10^{-3} | 2.6 | 77.2 |
| I | 2.00 | 222.2 | 111.0 | 1.44×10^{-3} | 3.3 | 90.4 |
| I | 5.00 | 410.0 | 81.8 | 1.44×10^{-3} | 5.0 | 122.9 |
| II | 0.25 | 65.5 | 261.9 | 2.35×10^{-3} | 3.8 | 62.9 |
| II | 4.00 | 399.4 | 99.9 | 2.08×10^{-3} | 5.9 | 146.3 |
| III | 0.25 | 150.0 | 600.0 | 28.28×10^{-3} | 22.5 | 329.9 |
| III | 4.00 | 876.9 | 219.2 | 22.07×10^{-3} | 34.3 | 704.6 |

array [Fig. 1(a)]. Each camera images a fall distance of ~ 30 mm at a nominal resolution of $6.75 \mu\text{m px}^{-1}$. The apparatus allows us to image individual solid 0.1–5 mm particles settling in quiescent air. See the Supplemental Material [45] for a complete description of the setup.

We used the Photonic Professional GT 3D printer (Nanoscribe GmbH) with submicrometer printing resolution to print submillimeter-sized spheroids with mass density $\rho_p = 1200 \text{ kg m}^{-3}$ [49]. Three size groups of spheroids were produced (Table I), with different aspect ratios $\lambda = a_{\parallel}/a_{\perp}$ ($2a_{\parallel}$ is the length of the particle symmetry axis, and $2a_{\perp}$ is the perpendicular diameter). Three-dimensional scans of the particle shape using a 3D laser-scanning microscope (VK-X200K, Keyence) show that the unevenness in the surface features of the spheroids is negligible (Fig. S2 in the Supplemental Material [45]). In total, we carried out between 9 and 22 measurements per particle shape and size, resulting in a total of 170 successful experimental runs where the particle was in sharp focus for all four cameras. Figure 1(b) shows recorded images of a prolate spheroid ($2a_{\parallel} = 410$, $2a_{\perp} = 82$) μm as it falls in the settling chamber. Figures S3 and S4 in the Supplemental Material [45] contain recorded images of all particles in Table I.

Figure 1(b) indicates that the orientation of the particle oscillates as it settles, in sharp contrast with previous experiments in liquids, where the alignment is monotonic [13,33,37,38,40]. To explain the oscillations observed here, we developed a theoretical model that includes the effect of particle inertia.

Model.—Since the particle-to-fluid mass-density ratio \mathcal{R} is large, one suspects that the observed oscillations in the angular dynamics are due to particle inertia. This

expectation is consistent with a recent theoretical study [27] of tilt-angle fluctuations of small particles in turbulence. However, we cannot directly apply the model from Ref. [27], because that model was derived assuming $\text{Re}_p \ll 1$, whereas our particles have Re_p of order 10. Therefore, we developed a theoretical description that extends the validity of the $\text{Re}_p \ll 1$ model. Specifically, we modified the fluid-inertia contributions to the hydrodynamic force and torque by introducing two scalar functions C_F and C_T that depend on the settling speed, determined using *ab initio* simulations of spheroids fixed in a uniform flow [40,50–54]. Details are given in Appendix A. As shown below, the new model accurately describes the experimental results and highlights the key significance of particle inertia. The model has three nondimensional parameters (Appendix C): the aspect ratio $\lambda = a_{\parallel}/a_{\perp}$, the nondimensional particle volume $\mathcal{V} = gV_p/\nu^2$, where g is the gravitational acceleration and $V_p = (4\pi/3)a_{\perp}^2 a_{\parallel}$ is the particle volume, and the mass-density ratio $\mathcal{R} = \rho_p/\rho_f$. These parameters determine the steady-state settling speed v_g^* and thus Re_p . For small settling speeds, $\text{Re}_p \approx (1/6\pi)\mathcal{R}\mathcal{V}$, up to a λ -dependent factor of order unity. For oblate disks, particle inertia can be parametrized by a nondimensional inertia ratio J^* . It is related to our nondimensional parameters by $J^* = (\pi/64)\mathcal{R}\lambda$ (Appendix C). Our J^* values are at least 2 orders of magnitude larger than for disks settling in water [28,34,55] and larger than in [35] by a factor ~ 2 .

Results.—The experimental results are compared with model predictions in Fig. 2. Figure 2(a) shows how the angle between the particle-symmetry vector and gravity (the tilt angle φ) decays to the steady value $\varphi^* = 0$ for disks and $\varphi^* = (\pi/2)$ for rods. The decay is oscillatory, as opposed to the behavior in water [13,32] where the decay is monotonic and the angular dynamics is overdamped (particle inertia is negligible). This is the case when the damping time τ_{ω} of the angular velocity is smaller than the decay time $\tau_{\varphi} \sim \nu/[v_g^*]^2$ of the tilt angle [33], which happens when $\mathcal{R}^3\mathcal{V}^2 \ll 1$ (Appendix C).

Figure 2(b) demonstrates that the model captures the observed settling dynamics very well. The largest disagreement is in the decay rate, which is hard to measure, especially for nearly spherical particles. The white markers in the bottom panel show selected experiments where the decay was best fitted by an exponential. The smaller scatter of these data points, closer to the theory, suggests that systematic errors in extracting the data provide the most likely explanation of differences between theory and experiments. Figure 2 reveals good agreement over the whole range of Re_p and λ covered by our experiments. We mention that differences between model and experiment are expected to grow at larger Re_p , because the determination of the inertial torque becomes less reliable beyond $\text{Re}_p \approx 30$ [54].

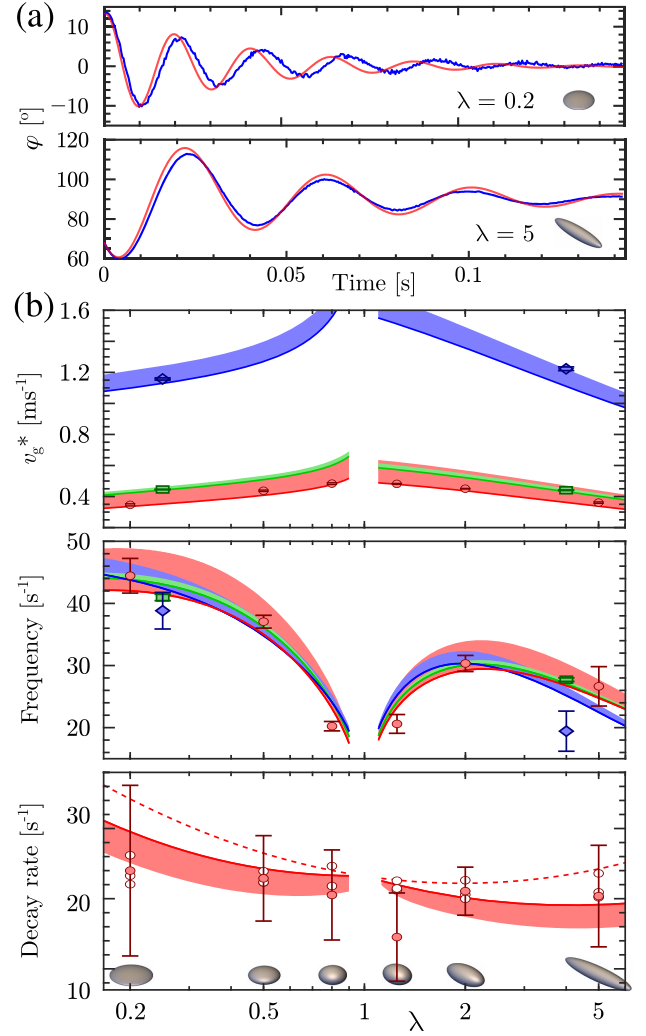


FIG. 2. Comparison between experiments and theory. (a) Time evolution of tilt angle φ from experiment (blue) and its model prediction (red) for spheroids with aspect ratios $\lambda = 0.2$ and 5 from group I (Table I). (b) Steady-state settling speed v_g^* , frequency, and decay rate of the tilt-angle oscillations as functions of the aspect ratio λ . Markers show averages obtained for all experiments with error bars indicating 95% confidence bounds for groups I (red circles), II (green squares), and III (blue diamonds) (Table I). Solid lines show large-time asymptotes from a linear-stability analysis of the model described in Appendix A. Shaded regions indicate how much the theoretical predictions change as the measured settling speed varies along the particle trajectory. See Appendixes A and B for details. Dashed lines show results of a linear-stability analysis of a harmonic-oscillator approximation, Eq. (D2) in Appendix D.

To develop a qualitative understanding of the oscillations, we simplified the model further, assuming that $\delta\varphi = \varphi - \varphi^*$ remains small and that the settling speed is large. In this limit we obtain a harmonic-oscillator equation for $\delta\varphi$, namely, $\delta\ddot{\varphi} + \delta\dot{\varphi} + (V_g^*)^2 C_T |h(\lambda)| \mathcal{R}^3 \mathcal{V}^2 \delta\varphi = 0$ in nondimensional units (Appendix D). In particular, V_g^* is a nondimensional settling speed $\propto v_g^*/(g\tau_p)$, and $h(\lambda)$ is a

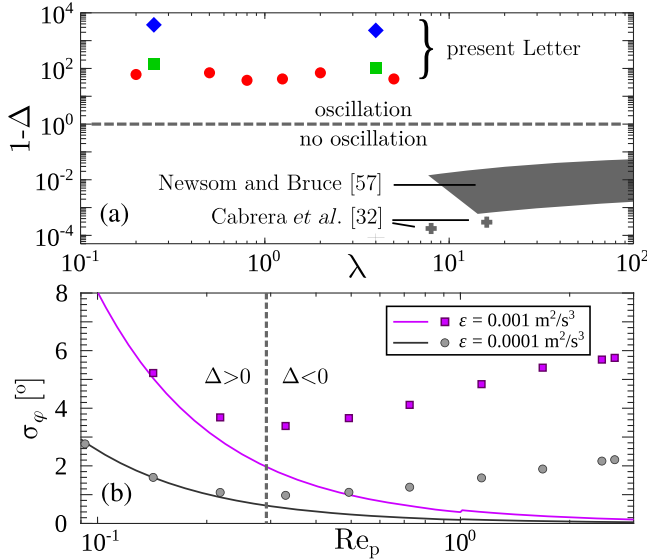


FIG. 3. (a) Bifurcation diagram. The dashed horizontal line distinguishes decay without oscillations ($\Delta > 0$) from decay with oscillations ($\Delta < 0$). Particles from group I in Table I are shown as red circles; group II as green squares; group III as blue diamonds; particles from Ref. [32] as +; fibers from Ref. [57] as a gray region. We approximated cylindrical fibers as slender prolate spheroids and estimated Δ by setting $C_T = C_F = 1$, since the corresponding Re_p are very small. (b) Standard deviation of tilt-angle fluctuations for spheroids settling in weakly turbulent air with dissipation rate ε , as a function of Re_p . Shown are simulation results of the model described in Appendix E in symbols, for spheroids with $\lambda = 0.2$, but different volumes V_p . Solid lines correspond to the overdamped approximation, neglecting particle inertia [Eq. (S6) in the Supplemental Material [45]]. The harmonic-oscillator bifurcation ($\Delta = 0$) is shown as a dashed vertical line.

shape-dependent function, shown in Fig. S6 [45]. For $Re_p \ll 1$ and $|\delta\varphi| \ll 1$, this equation simplifies to the form given in Refs. [27,33,56]. Linear-stability analysis of the harmonic-oscillator approximation shows that the particles approach alignment with an exponential decay, with decay rate $\mu_{\pm} = -\frac{1}{2} \pm \frac{1}{2} \sqrt{\Delta}$, with discriminant $\Delta = 1 - 4(V_g^*)^2 C_T |h(\lambda)| \mathcal{R}^3 \mathcal{V}^2$. The nondimensional steady-state settling speed V_g^* is of order unity. For all particles in our experiments, the values of $|h(\lambda)| \mathcal{R}^3 \mathcal{V}^2$ were large enough to ensure that $\Delta < 0$, as shown in Fig. 3(a). A qualitative change occurs when Δ becomes positive: then the particle orientation relaxes without oscillation. The expression for Δ shows that this bifurcation cannot occur in the overdamped limit $\mathcal{R}^3 \mathcal{V}^2 \ll 1$. We conclude that the bifurcation is due to particle inertia.

Now consider the very slender fibers measured in Ref. [57]. The asymptotic form of $|h(\lambda)|$ for large λ implies that $|h(\lambda)| \mathcal{R}^3 \mathcal{V}^2 \propto a_{\perp}^6$, disregarding factors of $\log \lambda$. It follows that, for $\mathcal{R} \sim 1000$, only fibers with a_{\perp} larger than $\sim 20 \mu\text{m}$ can oscillate. This explains why the fibers with diameters $\sim 10 \mu\text{m}$ used in Ref. [57], represented by the gray

region in Fig. 3(a), did not oscillate. We conclude that the angular dynamics of slender fibers in the atmosphere can be very different from that of particles of moderate aspect ratios. In case of very slender disks, $|h(\lambda)| \approx 7 \times 10^{-5} \lambda$, so the parameter combination $|h(\lambda)| \mathcal{R}^3 \mathcal{V}^2$ depends on particle geometry as $(a_{\perp} \sqrt{\lambda})^6$. Our estimates indicate that oscillations are observable for thin disks when $a_{\perp} \sqrt{\lambda}$ is larger than $\sim 20 \mu\text{m}$. This condition is very well fulfilled for the oblate particles in Table I, as well as for a large class of ice crystals [6]. A potential shortcoming of this analysis is that the forces and torques acting on thin disks have not been thoroughly tested for values significantly smaller than $\lambda \sim 0.1$ [52,54].

In turbulence, tilt-angle fluctuations are determined by balancing the inertial relaxation described above with the effect of turbulent fluid-velocity gradients that upset alignment. Typical Kolmogorov times for weak atmospheric turbulence $\tau_K \sim (\nu/\varepsilon)^{1/2} \sim 0.4\text{--}0.04 \text{ s}$ for the dissipation rate per unit mass ε from 10^{-4} to $10^{-2} \text{ m}^2/\text{s}^3$ [6] are of the same order as the timescales in Fig. 2, indicating that particle inertia can significantly increase the randomizing effect of turbulence, just as for small spherical particles, where particle inertia matters most for Stokes numbers of order unity and larger [15,58–60]. To describe the effect of turbulence, we added a stochastic forcing [60] to our model (Appendix E). Figure 3(b) summarizes the results. It shows the standard deviation σ_{φ} of the tilt-angle fluctuations for small turbulent dissipation rate, obtained by simulations of the model from Appendix E. Also shown is the overdamped approximation obtained by neglecting translational and rotational accelerations [Eq. (S6) in the Supplemental Material [45]]. In Fig. 3(b), Re_p was varied by changing the particle volume, keeping all other parameters the same. For small Re_p , simulations and overdamped theory agree, so particle inertia has no effect. As Re_p grows, σ_{φ} decreases at first, because the fluid-inertia torque aligns the particle more strongly as the settling speed increases. At the same time, a difference between simulations and overdamped theory develops: particle inertia enhances the tilt-angle fluctuations.

At still larger Re_p , σ_{φ} starts to increase again, forming a characteristic minimum. This can be understood in terms of the harmonic-oscillator approximation: the minimum in Fig. 3(b) occurs at a critical value of Re_p (details in the Supplemental Material [45]) where Δ becomes negative, indicating that the increase is due to the bifurcation described above, causing transient oscillations that result in larger angular fluctuations. The bifurcation occurs when Green's function of the harmonic-oscillator kernel becomes oscillatory, in the same way as without turbulence. The critical Re_p where this happens is much smaller than the particle Reynolds numbers where bistability [35] or fluttering [34,36] is observed. We remark that a preliminary analysis suggests that our model may also explain the

bistable angular dynamics observed in Ref. [35]. Also, dealing with more complex shapes is an important challenge. Ice crystals, for example, may be hollow or lack fore-aft symmetry [61]. This may give rise to additional torques [13,62].

In summary, our experiments and model calculations show that particle inertia has a strong effect on the angular dynamics of atmospheric particles, generally enhancing the orientation fluctuations of settling atmospheric particles, not only in still but also in turbulent air. This causes increased settling velocities and lateral drift, in contrast to the drift-free pattern observed for steadily settling particles in liquids. Orientation fluctuations also affect the rate at which nonspherical particles collide [15] or fragment, a process important for secondary ice particle production [63,64]. In addition, fluctuations in the orientation of ice crystals affect the radiative properties of ice-laden clouds, for example, by reducing cloud albedo when solar radiation is parallel to gravity.

Conclusions.—We identified the key importance of particle inertia for the motion of nonspherical atmospheric particles. Our results, made possible by the concurrent development of a unique experimental setup and by a reliable modeling strategy, show that heavy spheroids settling in air at $Re_p \sim 1\text{--}30$ (values typical for atmospheric particles) approach their stable orientation through decaying oscillations. We demonstrated that this behavior is a consequence of particle inertia. This physical effect must therefore be accounted for in models of important atmospheric processes, such as the radiative properties and evolution of ice-laden clouds, as well as residence times and dispersion ranges of volcanic ash or microplastics in the atmosphere.

T. B. was funded by the German Research Foundation (DFG) Walter Benjamin Position (Project No. 463393443). J. G. was supported by funding from the European Union Horizon 2020 Research and Innovation Program under the Marie Skłodowska-Curie Actions, Grant Agreement No. 675675. K. G. was supported by a grant from Vetenskapsrådet (No. 2018-03974). B. M. was supported by Vetenskapsrådet (Grant No. 2021-4452) and acknowledges a Mary Shepard B. Upson Visiting Professorship with the Sibley School of Mechanical and Aerospace Engineering at Cornell. Statistical-model simulations were performed on resources provided by the Swedish National Infrastructure for Computing (SNIC). This research was also supported in part by the National Science Foundation under Grant No. NSF PHY-1748958. We thank J. L. Pierson for pointing out Refs. [41,57] to us.

Appendix A: Model for Re_p up to ~ 30 .—The dynamics of a settling particle is determined by Newton's equations for translation and rotation,

$$\frac{d}{dt}\mathbf{x} = \mathbf{v}, \quad m_p \frac{d}{dt}\mathbf{v} = \mathbf{F}_h + m_p \mathbf{g}, \quad (\text{A1a})$$

$$\frac{d}{dt}\mathbf{n} = \boldsymbol{\omega} \wedge \mathbf{n}, \quad \frac{d}{dt}[\mathbb{J}_p(\mathbf{n})\boldsymbol{\omega}] = \mathbf{T}_h. \quad (\text{A1b})$$

Here \mathbf{x} is the particle position, \mathbf{v} its velocity, \mathbf{n} is a unit vector parallel to the symmetry axis of the particle, and $\boldsymbol{\omega}$ is the angular velocity of the particle. Its mass is m_p , and \mathbb{J}_p is the particle-inertia tensor [65]. The gravitational acceleration is denoted by \mathbf{g} .

The main difficulty is to determine the hydrodynamic force \mathbf{F}_h and torque \mathbf{T}_h . For $Re_p \ll 1$, they can be determined in perturbation theory [9,11,66,67]. For larger Re_p —as in the experiment—one can parametrize forces and torques on a spheroid in uniform flow using *ab initio* computer simulations [52,53]. The conclusion is generally that force and torque can be parametrized by introducing empirically determined correction factors in the perturbative equations of motion. Here we use

$$\mathbf{F}_h = \mathbf{F}_h^{(0)} + C_F \mathbf{F}_h^{(1)}, \quad \mathbf{T}_h = \mathbf{T}_h^{(0)} + C_T \mathbf{T}_h^{(1)}, \quad (\text{A2})$$

with correction factors $C_F(Re_p, \lambda)$ and $C_T(Re_p, \lambda)$. $\mathbf{F}_h^{(0)} = -(m_p/\tau_p)\mathbb{A}\mathbf{v}$ and $\mathbf{T}_h^{(0)} = -(m_p/\tau_p)\mathbb{C}\boldsymbol{\omega}$ are Stokes force and torque in a quiescent fluid [10,65], with particle response time $\tau_p = (2\rho_p/9\rho_f)(a_{\parallel}a_{\perp}/\nu)$ and resistance tensors $\mathbb{A}(\mathbf{n}, \lambda)$ and $\mathbb{C}(\mathbf{n}, \lambda)$ [Eqs. (4) and (7) in [33]]. The Re_p corrections are $\mathbf{F}_h^{(1)} = -(m_p/\tau_p)(3/16)(a_{\perp}v/\nu)(3\mathbb{A} - \mathbb{I}(\hat{\mathbf{v}} \cdot \mathbb{A}\hat{\mathbf{v}}))\mathbb{A}\mathbf{v}$ [66], where \mathbb{I} is the unit matrix, $\hat{\mathbf{v}} = \mathbf{v}/v$, $v = |\mathbf{v}|$, and $\mathbf{T}_h^{(1)} = F(\lambda)(m_p/6\pi)(a^3v^2/a_{\perp}\nu)(\mathbf{n} \cdot \hat{\mathbf{v}})(\mathbf{n} \wedge \hat{\mathbf{v}})/\tau_p$ [9,11], with $a = \max(a_{\parallel}, a_{\perp})$. For spheroids, the shape factor $F(\lambda)$ is given in Eqs. (4.1) and (4.2) of Ref. [67]. For $C_F = C_T = 1$, Eq. (A2) simplifies to known expressions for $Re_p \ll 1$ [27].

Equation (A2) yields good results for \mathbf{F}_h up to $Re_p \sim 100$, for prolate particles with moderate λ [53], and there is similar qualitative agreement for oblate particles [52]. We determined $C_F(Re_p, \lambda)$ from interpolations of *ab initio* simulation results for fixed Re_p and λ for oblate [52] and prolate [53] spheroids as follows. The full model [Eqs. (A1) and (A2)] has 11 dimensions. Since \mathbf{x} is slaved to the other variables, it is sufficient to analyze the eight-dimensional system for \mathbf{v} , $\boldsymbol{\omega}$, and \mathbf{n} . In the experiments, the particles settled with speeds close to the steady-state settling speed. Therefore, it suffices to evaluate C_F at the steady state

$$\mathbf{v}^* = v_g^* \hat{\mathbf{g}}, \quad \boldsymbol{\omega}^* = 0, \quad \varphi^* = 0, \frac{\pi}{2}. \quad (\text{A3})$$

Rotational symmetry dictates that the polar angle θ^* can take any value. Solving Eqs. (A1) and (A2) with a given (not yet known) value of C_F , we find

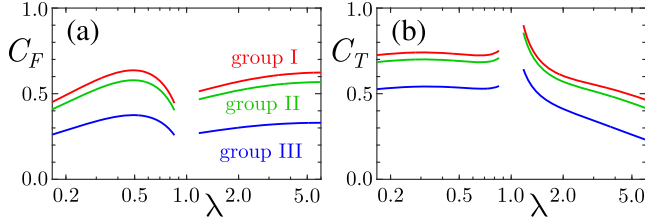


FIG. 4. Empirical coefficients C_F and C_T in Eq. (A2) for the parameters in Fig. 2, obtained as described in Appendix A. (a) Force coefficient C_F as a function of aspect ratio λ . The groups refer to Table I. (b) Torque coefficient C_T .

$$v_g^* = \frac{4\nu}{3A^{(g)}a_{\perp}C_F} \left(\sqrt{1 + \frac{3}{2}C_F \frac{a_{\perp}g\tau_p}{\nu}} - 1 \right). \quad (\text{A4})$$

Here $A^{(g)}$ is the component of the translational resistance tensor \mathbb{A} in the direction of gravity, for a particle falling with its steady-state orientation φ^* . We used Eq. (A4) to evaluate the Reynolds number $\text{Re}_p = av_g^*(C_F)/\nu$, with $a = \max\{a_{\perp}, a_{\parallel}\}$. Since C_F depends on Re_p , and Re_p in turn depends on C_F through $v_g^*(C_F)$, we solved the resulting implicit equation numerically to find the desired value of C_F . The results are shown in Fig. 4(a).

We determined $C_T(\text{Re}_p, \lambda)$ by interpolating the data in Refs. [52,53], using Re_p determined as described above. The results are shown in Fig. 4(b), and they are consistent with the *ab initio* simulations from Ref. [54].

It is not guaranteed that the model works outside the tested parameter range, for example, for very thin disks or for very nearly spherical particles. Therefore, we do not report numerical values for λ close to unity in Figs. 2 and 4. As mentioned above, we determined the functions $C_F(\text{Re}_p, \lambda)$ and $C_T(\text{Re}_p, \lambda)$ only near the steady state, for small $\delta\varphi = \varphi - \varphi^*$ (where φ is the tilt angle and $\varphi^* = 0, (\pi/2)$ is its steady-state value). This is sufficient as long as the dynamics does not depart too far from the steady state. Figures 2(a) and S5 [45] show that this works very well. The small drift of the angular dynamics in Fig. 2(a) may be due to inaccuracies in C_F or C_T . The accuracy of the model could be improved by introducing correction matrices \mathbb{C}_F and \mathbb{C}_T in Eq. (A2), instead of scalars, with elements that depend on φ , in addition to Re_p and λ .

Appendix B: Fitting the model to experimental data.— This appendix contains the details needed to reproduce the theoretical fits in Fig. 2. First, Eqs. (A1) and (A2) can be solved numerically for any initial condition \mathbf{v}_0 , \mathbf{n}_0 , and $\boldsymbol{\omega}_0$ (eight parameters). To reduce the number of parameters, we fitted only the initial tilt angle φ , its angular velocity $\dot{\varphi}$, the initial settling speed v_g , and the velocity component v_{\perp} perpendicular to gravity. We assumed steady-state values for the remaining parameters. As a result, the dynamics resides in a plane determined

by gravity and the direction of v_{\perp} . The red lines in Figs. 2(a) and S5 in the Supplemental Material [45] were obtained in this way. We see that the approximation works very well.

Second, to determine the shaded regions in Fig. 2(b), we perturbed the initial angular velocity and settling speed away from the above initial conditions, using typical experimental values for the particles from Table I.

Third, the solid lines in the top panel of Fig. 2(b) were obtained using Eq. (A4). The solid lines in the middle and bottom panels of Fig. 2(b) were determined from linear-stability analysis of the eight-dimensional dynamics of \mathbf{v} , $\boldsymbol{\omega}$, and \mathbf{n} . Linearizing the dynamics around the fixed point (A3), we obtained the eigenvalues describing exponential relaxation to the steady state. Two eigenvalues form a complex pair. The real part gives the decay rate and the imaginary part gives 2π times the frequency.

Appendix C: Nondimensional parameters.—We nondimensionalize velocities with $\tilde{v} \equiv g\tau_p/A^{(g)}$, obtained from Eq. (A4) in the limit of small settling speed, time with the angular-velocity relaxation time $\tau_{\omega} \equiv \tau_p J_{\perp}/(m_p C_{\perp})$, force with $m_p \tilde{v}/\tau_{\omega}$, and torque with $J_{\perp}/\tau_{\omega}^2$. Here $J_{\perp} = m_p[(1 + \lambda^2)/5]a_{\perp}^2$ is the moment of inertia of a spheroid around an axis perpendicular to its symmetry axis, and C_{\perp} is the rotational resistance coefficient around this axis [33]. In particular, the steady-state settling speed is nondimensionalized as $V_g^* = v_g^*/\tilde{v}$. In these nondimensional units, all terms in Eq. (A1) are of order unity, except for $F_h^{(1)} \sim (\rho_p/\rho_f)gV_p/\nu^2$ and $T_h^{(1)} \sim (\rho_p/\rho_f)^3(gV_p/\nu^2)^2$, where $V_p = (4\pi/3)a_{\perp}^2 a_{\parallel}$ is the volume of the particle. So there are two nondimensional parameters in addition to $\lambda = a_{\parallel}/a_{\perp}$: the mass-density ratio $\mathcal{R} = \rho_p/\rho_f$ and the nondimensional particle volume $\mathcal{V} = gV_p/\nu^2$. In the experiment, $\mathcal{R} = 996$, and $\mathcal{V} \approx 0.06$ (group I in Table I), $\mathcal{V} \approx 0.1$ (group II), and $\mathcal{V} \approx 1$ (group III). In the limit of small settling speeds, the parameters \mathcal{V} and \mathcal{R} are connected to Re_p by $\text{Re}_p \sim (1/6\pi)\mathcal{R}\mathcal{V}$, up to a λ -dependent prefactor.

The overdamped limit of the angular dynamics is obtained when $\tau_{\omega} \ll \tau_{\varphi}$, where $\tau_{\varphi} \sim \nu/[v_g^*]^2$ is the relaxation time of the tilt angle in this limit. So the overdamped limit corresponds to $\tau_{\omega}/\tau_{\varphi} \sim \mathcal{R}^3\mathcal{V}^2 \ll 1$.

Willmarth *et al.* [28] quantified particle inertia for settling disks by the phenomenological parameter $J^* = J_{\perp}^{(\text{cyl})}/J_f$, where $J_{\perp}^{(\text{cyl})} = (\pi/2)\rho_p\lambda a_{\perp}^5$ is the moment of inertia of a short cylinder around its axis perpendicular to the symmetry axis, and $J_f = \rho_f(2a_{\perp})^5$ is proportional to the moment of inertia of a fluid sphere with diameter $2a_{\perp}$. For oblate spheroids, this expression reduces to $J^* \propto \lambda\mathcal{R}$.

Appendix D: Harmonic-oscillator approximation.— The planar dynamics described in Appendix B can be

further simplified if $\delta\varphi$ is so small that its feedback upon the settling speed v_g can be neglected and if the transversal velocity is much smaller than the settling velocity. Then the tilt angle obeys a damped-pendulum equation. In the dimensionless units introduced in Appendix C, it reads

$$\dot{\varphi} = \omega, \quad \dot{\omega} = -\omega - \frac{1}{2}(V_g^*)^2 C_T h(\lambda) \mathcal{R}^3 \mathcal{V}^2 \sin(2\varphi). \quad (\text{D1})$$

The first term on the rhs of the equation for ω is the rotational damping due to particle inertia. The timescale is chosen so that the prefactor $|h(\lambda)|\mathcal{R}^3\mathcal{V}^2$ is unity. The dependence of the function $h(\lambda)$ on λ is shown in Fig. S6 [45]. For thin disks, $|h(\lambda)| \propto \lambda$. In this limit, the prefactor in the last term on the rhs of Eq. (D1) evaluates to $J^* \text{Re}_p^2$. This rationalizes the use of J^* to describe the effect of fluid inertia on settling disks [28].

Although Eq. (D1) is approximate, it captures the main features of the experimentally observed dynamics. The approach to the steady state is conveniently analyzed by linear-stability analysis. Linearization of Eq. (D1) yields the harmonic-oscillator approximation

$$0 = \delta\dot{\varphi} + \delta\dot{\omega} + (V_g^*)^2 C_T |h(\lambda)| \mathcal{R}^3 \mathcal{V}^2 \delta\varphi. \quad (\text{D2})$$

In the limit of $\text{Re}_p \ll 1$, a corresponding equation was considered earlier; see, for example, Eq. (45) in Ref. [33]. Equation (D2) implies that the tilt-angle fluctuation $\delta\varphi$ relaxes to zero exponentially, $\delta\varphi \sim a_+ \exp(\mu_+ t) + a_- \exp(\mu_- t)$, with eigenvalues $\mu_{\pm} = -1/2 \pm 1/2\sqrt{\Delta}$ and discriminant $\Delta = 1 - 4(V_g^*)^2 C_T |h(\lambda)| \mathcal{R}^3 \mathcal{V}^2$. The square root is real when $4(V_g^*)^2 C_T |h(\lambda)| \mathcal{R}^3 \mathcal{V}^2 \leq 1$ and purely imaginary otherwise. In the former case, relaxation toward the steady state is monotonic. In the latter case, it involves oscillations. We remark that $|h(\lambda)|$ takes small values (Fig. S6 [45]). This is compensated by $\mathcal{R}^3 \mathcal{V}^2 \gtrsim 10^5$ for the particles in Table I, with $\mathcal{R} \sim 10^3$. For these particles, Δ is negative. For much smaller ratios of particle-to-fluid mass densities, the condition $\Delta < 0$ is harder to satisfy.

The results of the harmonic-oscillator analysis are shown in Fig. 2 as dashed lines. In the top and middle panels, they are indistinguishable from the solid lines. For the exponential decay rate, by contrast, the harmonic-oscillator approximation differs from the solid lines. The bifurcation predicted by the harmonic-oscillator analysis is shown in Fig. 3 (dashed lines).

Appendix E: Effect of turbulence.—The effect of turbulence can be modeled by adding a stochastic forcing to the model described in Appendix A, representing the turbulent fluid velocity by a Gaussian random function $\mathbf{u}(\mathbf{x}, t)$ [Eq. (5) in Ref. [60]]. Since C_F and C_T in Eq. (A2) are approximated assuming small tilt

angles (Appendix A), we must assume that the turbulent dissipation rate is sufficiently small. The particle equations of motion (A1) and (A2) change in the presence of the turbulent flow $\mathbf{u}(\mathbf{x}, t)$. In the expressions for $\mathbf{F}_h^{(0,1)}$ and $\mathbf{T}_h^{(1)}$, the particle velocity \mathbf{v} is replaced by the slip velocity $\mathbf{v} - \mathbf{u}(\mathbf{x}, t)$ at the particle position \mathbf{x} . The second change is that there is an additional torque due to the gradients of the imposed flow [46]: $\mathbf{T}_j^{(0)} = (m_p/\tau_p)[\mathbb{C}\boldsymbol{\Omega}(\mathbf{x}, t) + \mathbb{H}:\mathbb{S}(\mathbf{x}, t)]$. Here $\boldsymbol{\Omega}(\mathbf{x}, t) = \frac{1}{2}[\nabla \times \mathbf{u}(\mathbf{x}, t)]$ is half the turbulent vorticity, and $\mathbb{S}(\mathbf{x}, t)$ is the strain-rate matrix, the symmetric part of the matrix of fluid-velocity gradients. The tensors \mathbb{C} and \mathbb{H} depend on particle shape. For spheroids, they are given in Eq. (7) of Ref. [33]. The colon symbol represents a double contraction of indices [10].

*T. B., J. S., and K. G. contributed equally to this work.

†Corresponding author: gholamhossein.bagheri@ds.mpg.de

- [1] G. Bagheri and C. Bonadonna, On the drag of freely falling non-spherical particles, *Powder Technol.* **301**, 526 (2016).
- [2] E. Rossi, G. Bagheri, F. Beckett, and C. Bonadonna, The fate of volcanic ash: Premature or delayed sedimentation?, *Nat. Commun.* **12**, 1303 (2021).
- [3] S. Allen, D. Allen, V. R. Phoenix, Durántez Jimenez, A. Simonneau, S. Binet, and D. Galop, Atmospheric transport and deposition of microplastics in a remote mountain catchment, *Nat. Geosci.* **12**, 339 (2019).
- [4] S. Zhang, Y. Kang, S. Allen, D. Allen, T. Gao, and Sillanpää, Atmospheric microplastics: A review on current status and perspectives, *Earth-Sci. Rev.* **203**, 103118 (2020).
- [5] D. C. Cox and H. W. Arnold, Observations of rapid changes in the orientation and degree of alignment of ice particles along an Earth-space radio propagation path, *J. Geophys. Res.* **84**, 5003 (1979).
- [6] H. R. Pruppacher and J. D. Klett, *Microphysics of Clouds and Precipitation*, 2nd ed. (Springer, New York, 2010).
- [7] T. J. Garrett, S. E. Yuter, C. Fallgatter, K. Shkurko, S. R. Rhodes, and J. L. Endries, Orientations and aspect ratios of falling snow, *Geophys. Res. Lett.* **42**, 4617 (2015).
- [8] P. K. Wang, *Physics and Dynamics of Clouds and Precipitation* (Cambridge University Press, Cambridge, England, 2013).
- [9] R. G. Cox, The steady motion of a particle of arbitrary shape at small Reynolds numbers, *J. Fluid Mech.* **23**, 625 (1965).
- [10] J. Happel and H. Brenner, *Low Reynolds Number Hydrodynamics* (Martinus Nijhoff Publishers, Hague, 1983).
- [11] R. E. Khayat and R. G. Cox, Inertia effects on the motion of long slender bodies, *J. Fluid Mech.* **209**, 435 (1989).
- [12] G. A. Voth and Alfredo Soldati, Anisotropic particles in turbulence, *Annu. Rev. Fluid Mech.* **49**, 249 (2017).
- [13] A. Roy, R. J. Hamati, L. Tierney, D. L. Koch, and G. A. Voth, Inertial torques and a symmetry breaking orientational transition in the sedimentation of slender fibres, *J. Fluid Mech.* **875**, 576 (2019).

- [14] A. J. Baran, From the single-scattering properties of ice crystals to climate prediction: A way forward, *Atmos. Res.* **112**, 45 (2012).
- [15] A. Pumir and M. Wilkinson, Collisional aggregation due to turbulence, *Annu. Rev. Condens. Matter Phys.* **7**, 141 (2016).
- [16] M. B. Pinsky and A. P. Khain, Some effects of cloud turbulence on water-ice and ice-ice collisions, *Atmos. Res.* **47–48**, 69 (1998).
- [17] C. Siewert, R. P. J. Kunnen, and W. Schröder, Collision rates of small ellipsoids settling in turbulence, *J. Fluid Mech.* **758**, 686 (2014).
- [18] M. Z. Sheikh, K. Gustavsson, E. Leveque, B. Mehlig, A. Pumir, and A. Naso, Colliding ice crystals in turbulent clouds, *J. Atmos. Sci.* **79**, 2050 (2022).
- [19] E. Gavze and A. P. Khain, Gravitational collision of small nonspherical particles: Swept volumes of prolate and oblate spheroids in calm air, *J. Atmos. Sci.* **79**, 1493 (2022).
- [20] N. A. Krotkov, D. E. Flittner, A. J. Krueger, A. Kostinski, C. Riley, W. Rose, and O. Torres, Effect of particle nonsphericity on satellite monitoring of drifting volcanic ash clouds, *J. Quant. Spectrosc. Radiat. Transfer* **63**, 613 (1999).
- [21] M. I. Mishchenko, W. B. Rossow, A. Macke, and A. A. Lacis, Sensitivity of cirrus cloud albedo, bidirectional reflectance and optical thickness retrieval accuracy to ice particle shape, *J. Geophys. Res.* **101**, 16973 (1996).
- [22] V. Noel and H. Chepfer, Study of ice crystal orientation in cirrus clouds based on satellite polarized radiance measurements, *J. Atmos. Sci.* **61**, 2073 (2004).
- [23] V. Noel and K. Sassen, Study of planar ice crystal orientations in ice clouds from scanning polarization lidar observations, *J. Appl. Meteorol.* **44**, 653 (2005).
- [24] C. D. Westbrook, A. J. Illingworth, E. J. O'Connor, and R. J. Hogan, Doppler lidar measurements of oriented planar ice crystals falling from supercooled and glaciated layer clouds, *Q. J. R. Meteorol. Soc.* **136**, 260 (2010).
- [25] V. Noel and H. Chepfer, A global view of horizontally oriented crystals in ice clouds from cloud-aerosol lidar and infrared pathfinder satellite observation (CALIPSO), *J. Geophys. Res.* **115** (2010).
- [26] A. Marshak, J. Herman, A. Szabo, K. Blank, S. Carn, A. Cede, I. Geogdzhayev, D. Huang, L. K. Huang, Y. Knyazikhin, M. Kowalewski, N. Krotkov, A. Lyapustin, R. McPeters, K. G. Meyer, A. Torres, and Y. Yang, Earth observations from DSCOVR EPIC instrument, *Bull. Am. Meteorol. Soc.* **99**, 1829 (2018).
- [27] K. Gustavsson, M. Z. Sheikh, A. Naso, A. Pumir, and B. Mehlig, Effect of particle inertia on the alignment of small ice crystals in turbulent clouds, *J. Atmos. Sci.* **78**, 2573 (2021).
- [28] W. W. Willmarth, N. E. Hawk, and R. L. Harvey, Steady and unsteady motions and wakes of freely falling disks, *Phys. Fluids* **7**, 197 (1964).
- [29] K. O. L. F. Jayaweera and R. E. Cottis, Fall velocities of plate-like and columnar ice crystals, *Q. J. R. Meteorol. Soc.* **95**, 703 (1969).
- [30] T. N. Swaminathan, K. Mukundakrishnan, and H. H. Hu, Sedimentation of an ellipsoid inside an infinitely long tube at low and intermediate Reynolds numbers, *J. Fluid Mech.* **551**, 357 (2006).
- [31] L. B. Esteban, J. S. Shrimpton, and B. Ganapathisubramani, Disks settling in turbulence, *J. Fluid Mech.* **883**, A58 (2020).
- [32] F. Cabrera, M. Z. Sheikh, B. Mehlig, N. Plihon, M. Bourgoïn, A. Pumir, and A. Naso, Experimental validation of fluid inertia models for a cylinder settling in a quiescent flow, *Phys. Rev. Fluids* **7**, 024301 (2022).
- [33] K. Gustavsson, M. Z. Sheikh, D. Lopez, A. Naso, A. Pumir, and B. Mehlig, Effect of fluid inertia on the orientation of a small prolate spheroid settling in turbulence, *New J. Phys.* **21**, 083008 (2019).
- [34] F. Auguste, J. Magnaudet, and D. Fabre, Falling styles of disks, *J. Fluid Mech.* **719**, 388 (2013).
- [35] A. Tinklenberg, M. Guala, and F. Coletti, Thin disks falling in air, *J. Fluid Mech.* **962**, A3 (2023).
- [36] U. Pesavento and Z. J. Wang, Falling paper: Navier-Stokes solutions, model of fluid forces, and center of mass elevation, *Phys. Rev. Lett.* **93**, 144501 (2004).
- [37] S. Kramel, Non-spherical particle dynamics in turbulence, Ph.D. thesis, Wesleyan University, 2017.
- [38] D. Lopez and E. Guazzelli, Inertial effects on fibers settling in a vortical flow, *Phys. Rev. Fluids* **2**, 024306 (2017).
- [39] S. Bounoua, G. Bouchet, and G. Verhille, Tumbling of inertial fibers in turbulence, *Phys. Rev. Lett.* **121**, 124502 (2018).
- [40] A. Roy, S. Kramel, U. Menon, G. A. Voth, and D. Koch, Orientation of finite Reynolds number anisotropic particles settling in turbulence, *J. Non-Newtonian Fluid Mech.* **318**, 105048 (2023).
- [41] R. K. Newsom and C. W. Bruce, Orientational properties of fibrous aerosols in atmospheric turbulence, *J. Aerosol Sci.* **29**, 773 (1998).
- [42] G. Q. Qi, G. J. Nathan, and R. M. Kelso, PTV measurement of drag coefficient of fibrous particles with large aspect ratio, *Powder Technol.* **229**, 261 (2012).
- [43] S. Kuperman, L. Sabban, and R. van Hout, Inertial effects on the dynamics of rigid heavy fibers in isotropic turbulence, *Phys. Rev. Fluids* **4**, 064301 (2019).
- [44] K. Gustavsson, J. Einarsson, and B. Mehlig, Tumbling of small axisymmetric particles in random and turbulent flows, *Phys. Rev. Lett.* **112**, 014501 (2014).
- [45] See Supplemental Material at <http://link.aps.org/supplemental/10.1103/PhysRevLett.132.034101> for detailed information regarding the experimental setup and the theoretical models, which contains Refs. [46–48].
- [46] G. B. Jeffery, The motion of ellipsoidal particles immersed in a viscous fluid, *Proc. R. Soc. A* **102**, 161 (1922).
- [47] R. Tsai, A versatile camera calibration technique for high-accuracy 3D machine vision metrology using off-the-shelf TV cameras and lenses, *IEEE Journal of robotics and automation* **3**, 323 (1987).
- [48] R. Clift and W. H. Gauvin, Motion of entrained particles in gas streams, *Can. J. Chem. Eng.* **49**, 439 (1971).
- [49] Y. Liu, J. H. Campbell, O. Stein, L. Jiang, J. Hund, and Y. Lu, Deformation behavior of foam laser targets fabricated by two-photon polymerization, *Nanomater. Nanotechnol.* **8**, 498 (2018).
- [50] R. Ouchene, M. Khalij, B. Arcen, and A. Tanière, A new set of correlations of drag, lift and torque coefficients for

- non-spherical particles at large Reynolds numbers, *Powder Technol.* **303**, 33 (2016).
- [51] H. I. Andersson and F. Jiang, Forces and torques on a prolate spheroid: Low-Reynolds number and attack angle effects, *Acta Mech.* **230**, 431 (2019).
- [52] R. Ouchene, Numerical simulation and modeling of the hydrodynamic forces and torque acting on individual oblate spheroids, *Phys. Fluids* **32**, 073303 (2020).
- [53] K. Fröhlich, M. Meinke, and W. Schröder, Correlations for inclined prolates based on highly resolved simulations, *J. Fluid Mech.* **901**, A5 (2020).
- [54] F. Jiang, L. Zhao, H. I. Andersson, K. Gustavsson, A. Pumir, and B. Mehlig, Inertial torque on a small spheroid in a stationary uniform flow, *Phys. Rev. Fluids* **6**, 024302 (2021).
- [55] P. Ern, F. Risso, D. Fabre, and J. Magnaudet, Wake-induced oscillatory paths of bodies freely rising or falling in fluids, *Annu. Rev. Fluid Mech.* **44**, 97 (2012).
- [56] J. D. Klett, Orientation model for particles in turbulence, *J. Atmos. Sci.* **52**, 2276 (1995).
- [57] R. K. Newsom and C. W. Bruce, The dynamics of fibrous aerosols in a quiescent atmosphere, *Phys. Fluids* **6**, 521 (1994).
- [58] K. Gustavsson and B. Mehlig, Statistical models for spatial patterns of heavy particles in turbulence, *Adv. Phys.* **61**, 1 (2016).
- [59] L. Brandt and F. Coletti, Particle-laden turbulence: Progress and perspectives, *Annu. Rev. Fluid Mech.* **54**, 159 (2022).
- [60] J. Bec, K. Gustavsson, and B. Mehlig, Statistical models for the dynamics of heavy particles in turbulence, *Annu. Rev. Fluid Mech.* **56**, 165 (2024).
- [61] A. J. Heymsfield, Laboratory and field observations of the growth of columnar and plate crystals from frozen droplets, *J. Atmos. Sci.* **30**, 1650 (1973).
- [62] F. Candelier and B. Mehlig, Settling of an asymmetric dumbbell in a quiescent fluid, *J. Fluid Mech.* **802**, 174 (2016).
- [63] A. Korolev and T. Leisner, Review of experimental studies of secondary ice production, *Atmos. Chem. Phys.* **20**, 11767 (2020).
- [64] T. Bhowmick, Y. Wang, M. Iovieno, G. Bagheri, and E. Bodenschatz, Supersaturation in the wake of a precipitating hydrometeor and its impact on aerosol activation, *Geophys. Res. Lett.* **47** (2020).
- [65] S. Kim and S. J. Karrila, *Microhydrodynamics: Principles and Selected Applications* (Butterworth-Heinemann, Boston, 1991).
- [66] H. Brenner, The Oseen resistance of a particle of arbitrary shape, *J. Fluid Mech.* **11**, 604 (1961).
- [67] V. Dabade, N. K. Marath, and G. Subramanian, Effects of inertia and viscoelasticity on sedimenting anisotropic particles, *J. Fluid Mech.* **778**, 133 (2015).